The Astrophysical Journal, 657:1026–1036, 2007 March 10

A *CHANDRA* SEARCH FOR CORONAL X-RAYS FROM THE COOL WHITE DWARF GD 356

Martin C. Weisskopf,[1] Kinwah Wu,[2] Virginia Trimble,[3,4] Stephen L. O'Dell,[1] Ronald F. Elsner,[1] Vyacheslav E. Zavlin,[1,5] and Chryssa Kouveliotou[1]

Received 2006 September 19; accepted 2006 November 9

ABSTRACT

We report observations with the *Chandra X-ray Observatory* of the single, cool, magnetic white dwarf GD 356. For consistent comparison with other X-ray observations of single white dwarfs, we also re-analyzed archival *ROSAT* data for GD 356 (GJ 1205), G99-47 (GR 290 = V1201 Ori), GD 90, G195-19 (EG 250 = GJ 339.1), and WD 2316+123, and archival *Chandra* data for LHS 1038 (GJ 1004) and GD 358 (V777 Her). Our *Chandra* observation detected no X-rays from GD 356, setting the most restrictive upper limit to the X-ray luminosity from any cool white dwarf: $L_X < 6.0 \times 10^{25}$ ergs s^{-1}, at 99.7% confidence, for a 1 keV thermal bremsstrahlung spectrum. The corresponding limit to the electron density is $n_0 < 4.4 \times 10^{11}$ cm^{-3}. Our re-analysis of the archival data confirmed the nondetections reported by the original investigators. We discuss the implications of our and prior observations for models of coronal emission from white dwarfs. For magnetic white dwarfs, we emphasize the more stringent constraints imposed by cyclotron radiation. In addition, we describe (in an Appendix) a statistical methodology for detecting a source and for constraining the strength of a source, which applies even when the number of source or background events is small.

Subject headings: methods: statistical — radiation mechanisms: thermal — stars: coronae — white dwarfs — X-rays: individual (GD 356)

1. INTRODUCTION

Several theorists (e.g., Zheleznyakov & Litvinchuk 1984; Serber 1990; Thomas et al. 1995) have suggested that single, cool, magnetic white dwarfs might have coronae. Some observers (Fontaine et al. 1982; Arnaud et al. 1992; Cavallo et al. 1993; Musielak et al. 1995, 2003) have previously searched for X-radiation that might be emitted by hot gas above a white dwarf photosphere. There were no persuasive detections, despite one false alarm, GR 290, in archival *Einstein* data (Arnaud et al. 1992). We here report another upper limit, more stringent than the previous ones, for the white dwarf star GD 356.

Three considerations motivated these X-ray searches: (1) the preponderance of magnetic white dwarfs among the X-ray-emitting cataclysmic variables; (2) the possibility that some features in the optical spectra of magnetic white dwarfs might be cyclotron resonances (Zheleznyakov & Litvinchuk 1984); and (3) the feeling that coronal heating is not so well understood that constraints from other kinds of stars would not be worthwhile. In the special case of GD 356, the presence of Balmer lines in emission implies at least a chromosphere, making more plausible the existence of a corona. Magnetic fields in most of the stars examined so far (including GD 356) are 1 MG or more, thought to be fossils from the white dwarfs' previous lives as Ap stars. More recent measurements of variable, weaker fields in some white dwarfs—the DBV GD 358 (Winget et al. 1994) and the DA LHS 1038 (Schmidt & Smith 1995)—suggest nonfossil magnetism. Calculations (Thomas et al. 1995) indicate that cool white dwarfs with convective envelopes can support α-ω dynamos capable of generating 100 kG fields.

Section 2 reviews recent theoretical considerations, and § 3 reviews limits from previous searches. Next, § 4 presents the results of our *Chandra* observations of GD 356, and § 5, our re-analysis of prior *Röntgensatellit* (*ROSAT*) and *Chandra* observations of GD 356 and other white dwarfs. Finally, § 6 discusses the implications of the new and re-analyzed results and emphasizes the importance of thermal cyclotron radiation in magnetic white dwarfs (cf. Zheleznyakov et al. 2004, and references therein).

2. MAGNETIC CORONAL ACTIVITY FROM WHITE DWARFS WITH A CONVECTIVE LAYER

White dwarfs are the class of compact objects that we presumably understand best. Nevertheless, several fundamental issues remain unresolved. For instance, are white dwarf magnetic fields all relic (fossil), or are there transient field components generated by dynamos? What excites the mysterious line emission from some white dwarfs? Are X-rays from white dwarfs, when detected, simply thermal emission from a deep photosphere?

All stars show a certain degree of magnetism. Quite often, coronal activity in nondegenerate stars demonstrates the presence of a magnetic field, presumably produced via magnetohydrodynamic (MHD) processes. In the canonical model, an α-ω dynamo in a convective stellar envelope generates the field; MHD waves or other forms of magnetic energy may then heat the corona. In contrast, the magnetic fields of degenerate stars, such as white dwarfs, may be fossil fields. Such a fossil field, together with a small, static atmospheric scale height, would lead one to conclude that such white dwarfs should not have coronae. However, some studies have challenged this conclusion. For example, theoretical arguments (Wesmael et al. 1980; Koester 2002) suggest that the cooler DA white dwarfs ($T_{\rm eff} < 18{,}000$ K) and DB white dwarfs ($T_{\rm eff} < 30{,}000$ K) could possess a convective zone—a necessary ingredient for coronal X-ray emission. Furthermore, differential rotation, if it occurs in white dwarfs (cf. Kawaler et al. 1999), might support a magnetic dynamo. As noted above, the magnetic field strength generated by an α-ω dynamo in a cool white dwarf might approach 100 kG (Thomas et al. 1995).

Most important is the presence of emission lines from some white dwarfs with no detectable companion. Among these, and thus especially interesting, are the H Balmer line emission from the

[1] NASA Marshall Space Flight Center, Huntsville, AL; martin@smoker.msfc.nasa.gov.
[2] Mullard Space Science Laboratory, University College London, Holmbury St. Mary, UK.
[3] Department of Physics and Astronomy, University of California, Irvine, CA.
[4] Las Cumbres Observatory, Goleta, CA.
[5] Research Fellow, NASA Postdoctoral Program (NPP).

TABLE 1
General Properties of GD 356 and Other Single White Dwarfs

Name (1)	R.A. (J2000.0)[a] (2)	Decl. (J2000.0)[a] (3)	μ_N[b] (arcsec y^{-1}) (4)	μ_W[b] (arcsec y^{-1}) (5)	D[c] (pc) (6)	Spectral Type[d] (7)	$T_{\rm eff}$[e] (K) (8)	B[e] (MG) (9)
LHS 1038.....	00 12 14.80	+50 25 21.4	−0.456	−0.548	11.0	DA8	6400	0.09
G99-47	05 56 25.47	+05 21 48.6	−0.446	−0.918	8.0	DAP9	5600	27
GD 90	08 19 46.38	+37 31 28.1	−0.112	−0.100	50	DAH5	11,000	10
G195-19	09 15 56.23	+53 25 24.9	−1.080	−1.116	10.3	DCP7	8000	100
GD 356	16 40 57.16	+53 41 09.6	−0.118	−0.186	21.1	DAH	7500	14
GD 358	16 47 18.39	+32 28 32.9	−0.166	+0.026	36.6	DBV2	24,000	0.0013
2316+123	23 18 45.10	+12 36 02.9	+0.102	−0.010	40	DAp	11,800	56

Note.—Units of right ascension are hours, minutes, and seconds, and units of declination are degrees, arcminutes, and arcseconds.
[a] J2000.0 coordinates are from the 2MASS All-Sky Catalog of Point Sources (Skrutskie et al. 2006) for epoch 2000.00.
[b] J2000.0 proper motion components μ_N and μ_W are from the Whole-Sky USNO-B1.0 Catalog (Monet et al. 2003).
[c] Distances are from the Yale Catalog of Trigonometric Parallaxes (van Altena et al. 1995), except (nonparallax) estimates for GD 90 and 2316+123 (Musielak et al. 1995).
[d] Spectral types are from the Villanova Catalog of Spectroscopically Identified White Dwarfs (McCook & Sion 1999).
[e] Surface effective temperatures and magnetic fields are from Jordan (2001), and references therein, except for GD 358 (Winget et al. 1994).

nearby (21.1 pc) white dwarf GD 356 (Greenstein & McCarthy 1985) and the metal lines from G227-5 and G35-26 (Provencal et al. 2005). For single white dwarfs, such emission lines indicate some chromospheric activity. Alternative models for the H emission lines in GD 356 include accretion of the interstellar medium and the presence of an interacting companion star or even a planet (Greenstein & McCarthy 1985; Li et al. 1998). The estimated luminosity of the Zeeman-split Hα emission lines of GD 356 is $\approx 2.1 \times 10^{27}$ ergs s^{-1}. Furthermore, the flat Balmer decrement [$f(\mathrm{H}\alpha)/f(\mathrm{H}\beta) \approx 1.2$; Greenstein & McCarthy 1985] excludes photoionization and recombination in an optically thin gas, suggesting instead a dense emission region with electron number density $n_e \approx 10^{14}$ cm^{-3} (Greenstein & McCarthy 1985). A possible cause of the chromospheric Balmer line emission is irradiation by UV/X-rays from a hot magnetic corona above the cooler white dwarf atmosphere. The presence of a white dwarf magnetic corona remains unverified, which motivated our *Chandra* observation. However, reported temporal variations of the magnetic field of (DBV) GD 358 (Winget et al. 1994) and of (DA) LHS 1038 (Schmidt & Smith 1995) are consistent with a magnetic corona.

In addition to facilitating the MHD dynamo process, a convective zone (Böhm & Cassinelli 1971; Arcoragi & Fontaine 1980) also results in acoustic wave, magnetic wave, and (nonwave) magnetic stress generation. Calculations show that the flux of such waves can be as large as $\approx 10^{10}$ ergs cm^{-2} s^{-1} (Arcoragi & Fontaine 1980; Musielak 1987). If the wave energy were to reach the white dwarf surface unabsorbed, it could provide a total luminosity $\approx 5 \times 10^{28}$ ergs s^{-1}. For purely acoustic modes, radiative damping and wave trapping attenuate most of this wave energy, such that very little reaches the white dwarf atmosphere (Musielak 1987; Musielak & Fontenla 1989). Hence, acoustic waves generated beneath the white dwarf photosphere cannot heat the corona (e.g., Ulmschneider 2003). In contrast, if the white dwarf is magnetic, but not so much as to suppress convection, transverse slow (magnetic wave) modes can propagate, carrying perhaps 60%–80% (Musielak 1987) of the wave energy into the stellar atmosphere. Thus, MHD wave or other magnetic energy flux remains a plausible mechanism for heating a white dwarf corona.

3. PREVIOUS X-RAY OBSERVATIONS

The detection of X-radiation from Sirius B (Mewe et al. 1975) established that white dwarfs are soft-X-ray sources. Subsequent *Einstein*, *EXOSAT*, and *ROSAT* observations (e.g., Musielak 1987; Kahn et al. 1984; Petre et al. 1986; Paerels & Heise 1989; Koester et al. 1990; Kidder et al. 1992; Barstow, et al. 1993) detected X-radiation from a number of hot ($T_{\rm eff} > 30{,}000$ K) white dwarfs. Thermal emission from the photosphere (Shipman 1976) accounts for the X-ray emission in all but one case: for (DO) KPD 0005+5106, optically thin thermal emission better fits the observed *ROSAT* data (Fleming et al. 1993), indicating a hot tenuous plasma layer enveloping the white dwarf. For KPD 0005+5106, the inferred temperature of the X-ray-emitting plasma is 0.2–0.3 MK, lower than the typical temperature of magnetic coronae around late-type stars, perhaps indicating a hot wind resembling those of O/B stars.

Searches with *Einstein* and *EXOSAT* (Fontaine et al. 1982; Arnaud et al. 1992) and with *ROSAT* (Cavallo et al. 1993; Musielak et al. 1995) for coronal X-rays from cool white dwarfs yielded no firm detections. For searches with the *ROSAT* PSPC, Cavallo et al. (1993) established X-ray upper limits for the white dwarfs G99-47 and G195-19; Musielak et al. (1995) for GD 90, GD 356, and WD 2316+123. Likewise, observations (Musielak et al. 2003) with the *Chandra* Advanced CCD Imaging Spectrometer (ACIS-S) of reportedly magnetically varying white dwarfs detected X-radiation neither from LHS 1038 nor from GD 358. Table 1 summarizes some relevant general properties of these white dwarfs: column (1) gives the name, columns (2) and (3), the epoch J2000.0 right ascension (R.A.) and declination (decl.), columns (4) and (5), the proper motion components, column (6), the distance, column (7), the spectral type, and columns (8) and (9), the surface effective temperature and magnetic field.

The previous searches determined upper limits to the X-ray luminosity for a thermal bremsstrahlung spectrum with negligible interstellar absorption. Assuming a coronal temperature of 11.6 MK (1.0 keV), Cavallo et al. (1993) obtained *ROSAT*-PSPC 99% confidence limits to the 0.1–2.5 keV luminosity of $<2.9 \times 10^{26}$ ergs s^{-1} for G99-47 and $<1.4 \times 10^{26}$ ergs s^{-1} for G195-19. Assuming a coronal temperature of 2.5 MK (0.215 keV), Musielak et al. (1995) obtained *ROSAT*-PSPC 99.7% confidence ($3\,\sigma$) limits to the 0.1–2.4 keV luminosity of $<7.8 \times 10^{27}$ ergs s^{-1} for GD 90, $<4.4 \times 10^{26}$ ergs s^{-1} for GD 356, and $<3.4 \times 10^{27}$ ergs s^{-1} for WD 2316+123. Under the same assumptions but using *Chandra*-ACIS-S observations, Musielak et al. (2003) found $<4.3 \times 10^{26}$ ergs s^{-1} for LHS 1038 and $<4.3 \times 10^{27}$ ergs s^{-1} for GD 358. These upper limits were comparable to the X-ray luminosities that Musielak et al. (2003) had predicted for LHS 1038

TABLE 2
X-Ray Observations of GD 356 and Other Single White Dwarfs

Name (1)	Observatory Used[a] (2)	Epoch[b] $t_{obs} - 2000$ (3)	Time (ks) (4)	m_T[c] (5)	Ω_T[c] (arcsec^2) (6)	m_R[c] (7)	Ω_R[c] (arcsec^2) (8)	$\mathcal{C}_{det}$[d] (%) (9)	$\bar{m}_S$[e] (10)	$\log(L_X)$[f] (cgs) (11)	$\log(n_0)$[g] (cgs) (12)
LHS 1038.....	*Chandra*	+0.97	5.88	0	3.14	2029	234,000	0	<5.0	<25.95	<11.72
G99-47.....	*ROSAT*	−7.75	9.28	44	25,500	85	45,200	30	<23.4	<26.21	<11.85
GD 90	*ROSAT*	−7.75	8.56	91	25,500	157	45,200	57	<40.0	<28.07	<12.78
G195-19	*ROSAT*	−7.69	6.99	90	25,500	195	45,200	5	<23.9	<26.57	<12.03
GD 356	*Chandra*	+5.39	31.8	0	3.14	5437	216,000	0	<5.0	<25.78	<11.64
GD 356	*ROSAT*	−7.99	28.2	234	25,500	413	45,200	52	<60.5	<26.99	<12.24
GD 358	*Chandra*	+1.79	4.88	0	3.14	2402	233,000	0	<5.0	<27.06	<12.28
2316+123	*ROSAT*	−8.08	9.12	44	25,500	61	45,200	88	<37.7	<27.83	<12.66

[a] *Chandra* observations used the ACIS-S instrument; *ROSAT* observations used the PSPC.
[b] Proper motion adjustment of coordinates requires epoch of X-ray observation relative to epoch of catalogued position.
[c] X-ray observation detected m_T and m_R events in Target T and Reference R apertures, of measure Ω_T and Ω_R, respectively.
[d] Source-detection confidence is the probability that the background contributes fewer than the observed number of events in the Target aperture (eq. [A8]).
[e] Upper limit to the expectation value of 0.1–2.4 keV source events is at (3 σ) 99.7% confidence (eq. [A22]).
[f] Calculated X-ray luminosity assumes thermal bremsstrahlung at $kT = 1$ keV.
[g] Calculated electron density at coronal base assumes thermal bremsstrahlung at $kT = 1$ keV, from a fully ionized plasma with $n_{He}/n_H = 0.1$, above an opaque white dwarf of radius 0.0105 $R_\odot = 7.34 \times 10^8$ cm and surface gravity $\log(g\,[\mathrm{cgs}]) = 8$.

and GD 358: 5×10^{26} ergs s^{-1} and 5×10^{27} ergs s^{-1}, respectively. For uniform comparison of results over a wider range of assumed parameters, we re-analyzed (§ 5 and Table 2) the relevant archived *Chandra* (§ 5.1) and *ROSAT* (§ 5.2) data.

4. THE *CHANDRA* OBSERVATION OF GD 356

We obtained a 31.8 ks *Chandra* observation (ObsID 4484, 2005 May 24) using the ACIS-S3 (back-illuminated) CCD in the faint, timed-exposure mode, with 3.141 s frame time. Background levels were nominal throughout the observation. Standard *Chandra* X-ray Center (CXC) processing (ASCDS version CIAO 3.2) provided level 2 event files. In analyzing data, we utilized events in pulse-invariant channels corresponding to 0.5–8.0 keV.

Our *Chandra* observation found no X-rays in a 1″ radius detect cell at the epoch 2005.39 position of GD 356 ($16^h40^m57.23^s$, $+53°41'8.6''$, after adjustment of the epoch J2000.0 coordinates for proper motion [Table 1]). The nearest detected X-ray source, No. 6 in Table 3, lies 46″ from GD 356. To determine

TABLE 3
Chandra-Detected Sources in the GD-356 Field

Source (1)	R.A. (J2000.0) (2)	Decl. (J2000.0) (3)	θ_{ext}[a] (arcsec) (4)	m_D[b] (5)	θ_{99}[c] (arcsec) (6)
1.....	16 40 45.029	+53 44 47.38	2.7	8.9	1.25
2.....	16 40 45.299	+53 45 13.15	3.1	13.6	1.18
3.....	16 40 53.706	+53 44 42.50	2.4	9.2	1.15
4.....	16 40 55.545	+53 40 25.24	1.3	22.0	0.69
5.....	16 40 56.104	+53 39 18.33	1.7	25.9	0.73
6.....	16 40 59.258	+53 41 59.41	1.2	36.4	0.66
7.....	16 41 00.438	+53 42 03.31	1.3	10.2	0.78
8.....	16 41 04.242	+53 40 20.98	1.6	7.3	0.94
9.....	16 41 05.997	+53 43 18.82	2.0	21.0	0.80
10.....	16 41 06.757	+53 37 52.85	3.3	30.6	0.94
11.....	16 41 07.650	+53 45 27.75	3.7	17.8	1.23
12.....	16 41 10.745	+53 44 36.43	3.2	16.5	1.13
13.....	16 41 13.050	+53 41 57.24	2.2	12.9	0.97
14.....	16 41 14.806	+53 41 41.18	2.4	12.6	1.02
15.....	16 41 15.481	+53 44 10.91	3.4	4559.0	0.61
16.....	16 41 16.876	+53 42 56.29	2.9	118.6	0.69
17.....	16 41 19.134	+53 44 11.29	3.9	32.1	1.03
18.....	16 41 21.033	+53 40 54.25	3.3	17.6	1.13
19.....	16 41 24.066	+53 41 48.86	3.8	8.2	1.71
20.....	16 41 30.445	+53 41 18.79	5.0	27.8	1.30
21.....	16 41 32.519	+53 36 40.09	8.4	17.8	2.49
22.....	16 41 33.184	+53 43 05.51	5.9	12.7	2.10
23.....	16 41 37.639	+53 39 57.65	6.9	8.5	2.93

Note.—Units of right ascension are hours, minutes, and seconds, and units of declination are degrees, arcminutes, and arcseconds.
[a] The extraction radius demarks the detect cell for collecting X-ray counts.
[b] An ACIS-S3 observation (ObsID 4484) acquired these detect-cell counts in 31.8 ks.
[c] This radius encloses the true position of the detected source at 99% confidence.

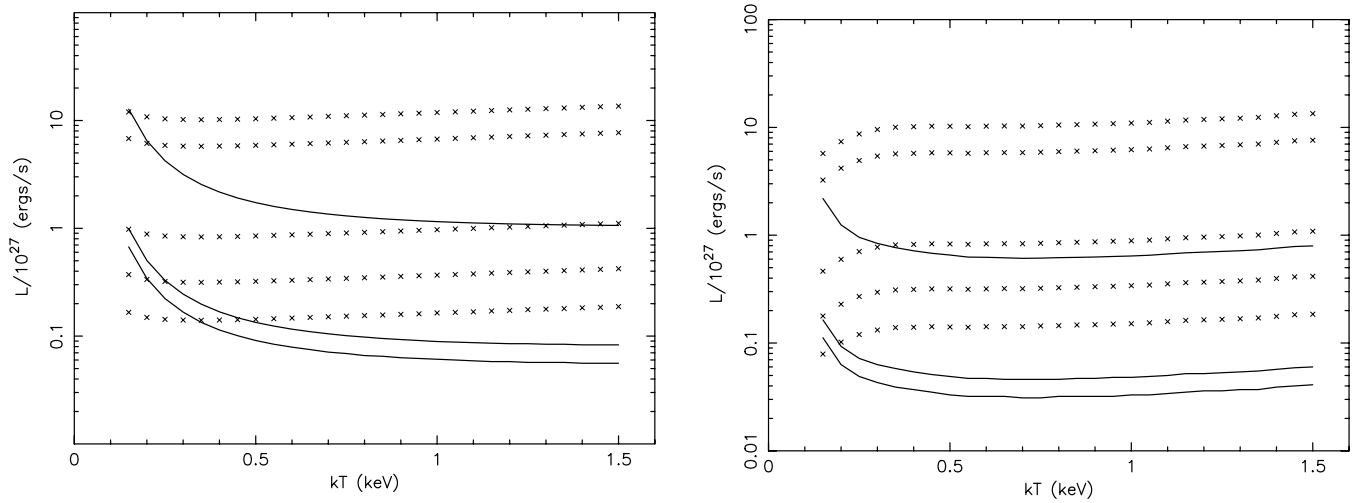

FIG. 1.—The 99.7% confidence upper limits to total X-ray luminosity vs. temperature for bremsstrahlung (*left panel*) and MEKAL (*right panel*) models. From lowest to highest, limits based on *Chandra* data (*solid lines*) are for GD 356, LHS 1038, and GD 358; those based on *ROSAT* data (*crosses*) are for G99-47, G195-19, GD 356, 2316+123, and GD 90.

the background, we "punched out" the detected X-ray sources eliminating all counts within a 20 σ radius of each position in Table 3. Table 2 summarizes the results for our *Chandra* observation of GD 356, as well as for our re-analysis (§ 5) of previous *Chandra* (§ 5.1) and *ROSAT* (§ 5.2) searches for X-ray emission from this and other single white dwarfs. Column (1) lists the name of the white dwarf, column (2), the observatory used, column (3), the epoch relative to J2000.0 (used to adjust for proper motion), and column (4), the integration time. Column (5) presents the number of detected counts m_T in the "Target" (detect) cell T and column (6), its solid angle Ω_T. Analogously, column (7) presents the number of detected counts m_R in the "Reference" region R and column (8), its solid angle Ω_R. Finally, columns (9), (10), (11), and (12) list, respectively, the confidence level for detection of a source (§ A2 of the Appendix), the 99.7% confidence upper limit on the expectation value of the number of source counts (§ A3 of the Appendix), and the corresponding limits on the X-ray luminosity (for a 1 keV thermal bremsstrahlung spectrum) and on the electron density, which follow from the analysis below. Owing to the very small (1″ radius) detect cell afforded by *Chandra*'s subarcsecond resolution, only 2 counts in the Target aperture would have constituted a (3 σ) 99.7% confidence detection for either of the three *Chandra* data sets! Neither of the three *Chandra* observations found an event in the detect cell.

A statistical analysis (Appendix A) of the data yields (eq. [A8]) the confidence level for detection of a source within the Target (detect) cell and (eq. [A22]) a 99.7% confidence upper limit to the expected number of source counts in the Target (detect) cell T. Before converting the source counts to a flux and luminosity, we correct for the fraction of the point-spread function (PSF) outside the detect cell. For *Chandra*, and almost any soft spectrum, about 90%[6] of the source photons for an on-axis source would lie within the chosen detect cell. To convert the resulting 5 count (4.5/0.9) limit to a flux, we calculated the redistribution matrix (rmf) and effective area (arf) functions appropriate to the location of GD 356 in the focal plane, using the *Chandra* CIAO 3.3 software tools `mkacisarmf` and `mkarf`, following the analysis thread[7] for creating these functions for a specific location. Assuming a column density $N_{\rm H} = 5 \times 10^{18}$ cm^{-2} and a thermal bremsstrahlung spectrum, we used XSPEC (v11.3.2)[8] with `abund` set to `wilm`, `xsect` set to `vern`, and `tbabs(bremss)` as the model. For each assumed value for the coronal temperature, we adjusted the model normalization until the absorbed flux produced 5.0 counts in the S3 detector in the observing time of the *Chandra* observation. Feeding this normalization into XSPEC, we used the `dummyrsp` feature to calculate the flux for 10^4 bins over the energy range 10^{-5}–100 keV. We used this approach to improve the accuracy of our flux calculations, since the instrument response is calculated over a more restricted energy range and with cruder energy bins. We then calculated fluxes over the band from 0.01 to 100 keV, now setting the column density to zero to obtain the unabsorbed flux.

The upper panel of Figure 1 plots the 3 σ upper limit to the total luminosity, as a function of coronal temperature, for our observation of GD 356 and for our re-analysis (§ 5) of previous white dwarf observations. The upper panel of Figure 2 shows the corresponding upper limit to the electron density for an effective emitting volume $4\pi R^2 H$, appropriate for a geometrically thin ($H \ll R$) transparent atmosphere of (exponential) scale height H around a sphere of radius R. For the ion density, we assume a fully ionized plasma of hydrogen and helium with $n_{\rm He}/n_{\rm H} = 0.1$, such that $\sum n_i Z_i^2 = 1.4 n_e$. The bremsstrahlung emissivity then scales as $1.4 n_e^2 = 1.4 n_0^2/2$, where n_0 is the electron density at the base of an isothermal corona. Note that only about half of the coronal emission emerges, due to photospheric absorption of most of the downward coronal flux. Using GD 356's 21.1 pc parallax distance (van Altena et al. 1995) and published *UBV* (Mermilliod & Mermilliod 1994) and *JHK* (Skrutskie et al. 2006) photometry, we obtain the photospheric temperature $T_s = 7840$ K and radius $R = 0.0105\ R_\odot = 7.34 \times 10^8$ cm. For the coronal scale height, we use $H = (2 \times 10^7\ {\rm cm}) kT/(1\ {\rm keV})$, corresponding to a surface gravity $\log(g\ [{\rm cgs}]) = 8$. The lower panels of Figures 1 and 2 display analogous limits for the `tbabs(mekal)` Mewe-Kaastra-Liedahl (MEKAL) model, with parameters as above, but with `abund` set to `lodd`.

Besides examining the white dwarf location for X-rays, we searched for X-ray sources anywhere on S3, employing techniques

[6] See http://asc.harvard.edu/proposer/POG/index.html.
[7] See http://cxc.harvard.edu/ciao/ahelp/mkacisrmf.html.
[8] See http://xspec.gsfc.nasa.gov.

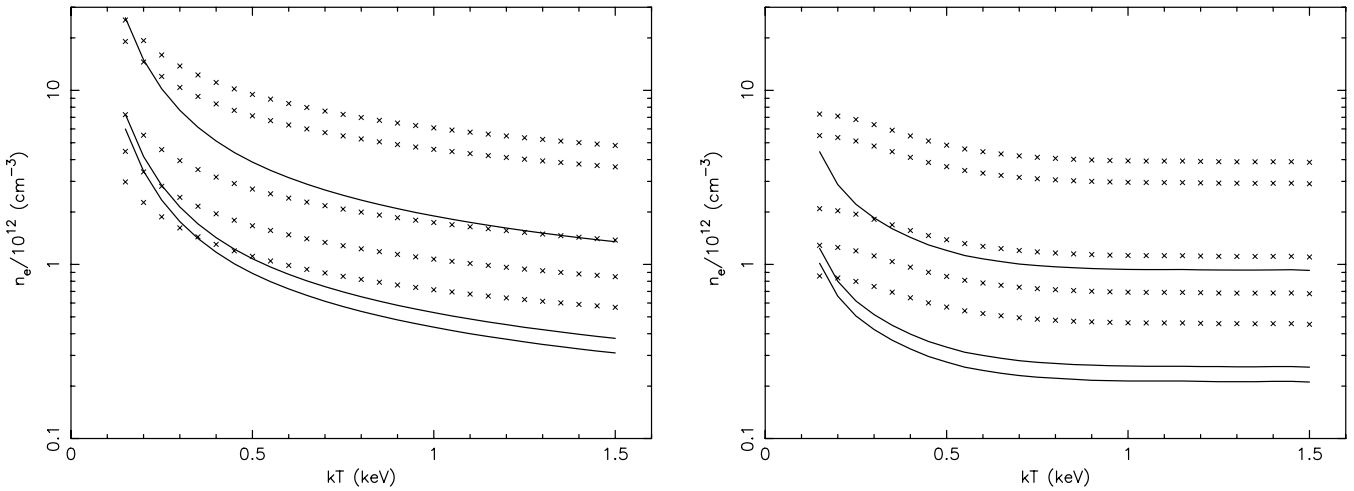

FIG. 2.—The 99.7% confidence upper limits to coronal electron density vs. temperature for bremsstrahlung (*left panel*) and for MEKAL (*right panel*) models. From lowest to highest, limits based *Chandra* data (*solid lines*) are for GD 356, LHS 1038, and GD 358; those based on *ROSAT* data (*crosses*) are for G 99-47, G 195-19, GD 356, 2316+123, and GD 90.

described in Tennant (2006). For the 31.8 ks *Chandra* observation, Table 3 lists the X-ray properties of the 23 detected sources, each designated with a source number in column (1). Columns (2)–(5) give, respectively, right ascension (R.A. [J2000.0]), declination (decl. [J2000.0]), extraction radius $\theta_{\rm ext}$, and approximate number of X-ray counts m_D detected from the source. The single-axis rms error in the X-ray source position is $\sigma_{\rm X} = [(\sigma^2_{\rm PSF}/m_D) + \sigma^2_{\rm sys}]^{1/2}$, where m_D is the approximate number of detected events above background, $\sigma_{\rm PSF}$ is the dispersion of the circular Gaussian that approximately matches the PSF at the source location, and $\sigma_{\rm sys}$ is a systematic error. Uncertainties in the plate scale[9] imply that $\sigma_{\rm sys} \approx 0.13''$; to be conservative, we set $\sigma_{\rm sys} = 0.2''$ (per axis). Column (6) gives the radial uncertainty $\theta_{99} = 3.03\sigma_{\rm X}$ in the X-ray position, i.e., $\chi^2_2 = 9.21 = 3.03^2$ corresponds to 99% confidence on 2 degrees of freedom for inclusion of the true source position.

5. RE-ANALYSIS OF PREVIOUS OBSERVATIONS

For consistent comparison of X-ray observations, we also re-analyzed certain prior *Chandra* (§ 5.1) and *ROSAT* (§ 5.2) observations of single cool white dwarfs. The *Chandra* observations used the ACIS-S instrument; the *ROSAT* observations, the PSPC.

[9] See http://asc.harvard.edu/cal/docs/cal_present_status.html#rel_spat_pos.

TABLE 4
Chandra-DETECTED SOURCES IN THE LHS-1038 FIELD

Source (1)	R.A. (J2000.0) (2)	Decl. (J2000.0) (3)	$\theta_{\rm ext}$[a] (arcsec) (4)	m_D[b] (5)	θ_{99}[c] (arcsec) (6)
1.....	0 12 05.742	+50 28 17.79	2.8	11.3	1.16
2.....	0 12 08.128	+50 30 16.70	4.6	10.1	1.86
3.....	0 12 10.118	+50 28 30.63	2.7	60.9	0.73
4.....	0 12 31.360	+50 32 16.93	8.1	35.5	1.75

NOTE.—Units of right ascension are hours, minutes, and seconds, and units of declination are degrees, arcminutes, and arcseconds.
[a] The extraction radius demarks the detect cell for collecting X-ray counts.
[b] An ACIS-S3 observation (ObsID 1864) acquired these detect-cell counts in 5.88 ks.
[c] This radius encloses the true position of the detected source at 99% confidence.

5.1. *Prior Chandra Observations*

We reprocessed and analyzed previous *Chandra* observations of the cool white dwarfs LHS 1038 (ObsID 1864, 5.88 ks) and GD 358 (ObsID 1865, 4.88 ks), in the same manner as for GD 356 (§ 4). Table 2 summarizes relevant parameters and results. Figure 1 shows the total luminosity (3 σ) 99.7% confidence limits for distances listed in Table 1. Figure 2 plots the corresponding upper limits to the electron density, approximating the radius of each white dwarf by that of GD 356 (§ 4).

As described above for our observation of the GD 356 field (§ 4), we also searched for X-ray sources in the S3 observations of the LHS 1038 and GD 358 fields. In the same form as Table 3, Tables 4 and 5 list X-ray sources detected on S3, for the LHS 1038 and GD 358 fields, respectively.

5.2. *ROSAT Observations*

Table 2 also summarizes our re-analysis of the *ROSAT*-PSPC observations, first analyzed by Cavallo et al. (1993) and by Musielak et al. (1995). For the re-analysis, we selected the

TABLE 5
Chandra-DETECTED SOURCES IN THE GD-358 FIELD

Source (1)	R.A. (J2000.0) (2)	Decl. (J2000.0) (3)	$\theta_{\rm ext}$[a] (arcsec) (4)	m_D[b] (5)	θ_{99}[c] (arcsec) (6)
1.....	16 46 55.620	+32 29 49.17	4.8	6.9	2.29
2.....	16 46 58.650	+32 29 30.20	3.9	9.6	1.64
3.....	16 47 07.418	+32 30 50.62	3.0	25.1	0.95
4.....	16 47 08.044	+32 25 17.23	2.7	17.2	0.99
5.....	16 47 13.515	+32 32 03.03	3.5	20.6	1.12
6.....	16 47 17.610	+32 33 15.56	4.8	25.3	1.31
7.....	16 47 18.628	+32 27 51.63	1.1	51.1	0.63
8.....	16 47 18.645	+32 29 16.22	1.4	13.3	0.76
9.....	16 47 26.652	+32 27 30.17	1.4	8.4	0.85
10.....	16 47 27.949	+32 27 37.51	1.5	13.0	0.80

NOTE.—Units of right ascension are hours, minutes, and seconds, and units of declination are degrees, arcminutes, and arcseconds.
[a] The extraction radius demarks the detect cell for collecting X-ray counts.
[b] An ACIS-S3 observation (ObsID 1865) acquired these detect-cell counts in 4.88 ks.
[c] This radius encloses the true position of the detected source at 99% confidence.

0.1–2.4 keV energy band, a Target region of 1.5′ (source extraction) radius, and an annular Reference region of 1.5′–2.5′ radius (for background estimation), as did Musielak et al. (1995). For sufficiently soft sources ($E < 0.5$ keV), most ($\geq$97%) of the flux from a source lies within the 1.5′ radius Target (detect) region (Boese 2000). Toward higher energies, the upper limits will be somewhat conservative because a decreasing fraction of source events appears in the Target aperture, while an increasing fraction appears in the Reference aperture. Furthermore, the *ROSAT* exposures are not sufficiently long to measure the background accurately. Appendix A describes a statistical methodology for dealing with these issues.

Following procedures described above (§ 4) but now using the *ROSAT*-PSPC response matrix, we established (3 σ) 99.7% confidence upper limits to the expected number of source counts and then converted those to flux and luminosity. For calculating luminosity, we used the distances listed in Table 1. Figure 1 plots the derived luminosity limit as a function of assumed temperature for the bremsstrahlung (*right panel*) and MEKAL (*left panel*) spectral models. Figure 2 shows the corresponding 3 σ upper limits to the electron density, again approximating the radius of each white dwarf by that of GD 356 (§ 4).

6. DISCUSSION

The objective of this investigation was to determine whether single cool white dwarfs emit X-radiation indicative of magnetic coronal activity. To assess the scientific implications of these null detections, we first (§ 6.1) discuss issues related to the formation of a magnetic corona around a white dwarf. We then (§ 6.2) examine the rather severe constraints that cyclotron emission lines and radiative loss impose on a corona around a cool magnetic white dwarf, such as GD 356. Finally (§ 6.3), we summarize our results and conclusions about hypothesized hot coronae around magnetic white dwarfs.

6.1. *Formation of a Corona*

The existence of coronae around single cool white dwarfs remains an unsettled issue. This, of course, motivated our search for X-ray evidence. Here we briefly address some questions relevant to the formation of a magnetic corona.

1. Is there a convection zone? Theoretical studies have indicated that convection can occur in white dwarfs for certain temperature ranges. Analyses of white dwarf atmospheric elemental abundance also evidence convective activity. Thus, it is quite plausible that some white dwarfs possess a convection zone that generates MHD waves.

2. How much MHD wave energy is generated in the convection zone? Calculations (Musielak 1987; Winget et al. 1994) have shown that the convection-generated wave flux could exceed 10^8 ergs cm^{-2} s^{-1} and may reach 10^{10} ergs cm^{-2} s^{-1} for DA white dwarfs and 10^{11} ergs cm^{-2} s^{-1} for DB white dwarfs.

3. What fraction of the wave energy is transmitted to the white dwarf surface? This fraction is uncertain. For white dwarfs with a substantial magnetic field ($B \approx 10^4$ G or higher), half the wave energy generated in the convection zone might reach the white dwarf atmosphere. If all the wave energy is converted into coronal X-rays, the expected luminosity will be $\approx 10^{27}$–10^{30} ergs s^{-1}. Our upper limit to the X-ray luminosity for GD 356 is an order of magnitude below 10^{27} ergs s^{-1} over most of the range of assumed temperatures. This implies either that the putative convection zone generates less wave energy, that the efficiency of wave transmission to the surface is smaller, or that a corona fails to form even if the wave energy reaches the white dwarf surface.

4. Can a magnetic corona form, given sufficient energy provided by the MHD wave or other energy stored in the magnetic field? The null detection of coronal X-rays from white dwarfs has led some (see, e.g., Musielak et al. 2005) to suggest that the emerging wave flux causes chromospheric activity rather than formation of a hot corona. An example of such chromospheric activity would be oscillations resulting from the response of the stellar atmosphere to propagating waves in the presence of a temperature inversion (Musielak et al. 2005). Whether waves generate chromospheric activity remains unverified. Nevertheless, a number of systems exhibit chromospheric activity. The luminosity of Hα emission lines in GD 356 is $\approx 1.8 \times 10^{27}$ ergs s^{-1} (see Greenstein & McCarthy 1985). Our *Chandra* observation eliminates the possibility that irradiation of the atmosphere by coronal X-rays powers the Balmer lines. Further, it is not clear that atmospheric oscillations can account for the luminosity of Balmer emission lines in GD 356.

While coronal X-radiation from cool ($T_{\rm eff} < 10{,}000$ K) magnetic white dwarfs remains undetected, X-radiation from hot optically thin thermal plasmas appears to occur from the very hot (1.2×10^5 K) white dwarf KPD 0005+5106. Now the question is this: without a magnetic corona, what supports the hot plasma envelope in the strong gravitational field of the white dwarf? Radiation driven envelopes, predicted for hot white dwarfs (Bespalov & Zheleznyakov 1990; Zheleznyakov et al. 1996), could provide this support. Provided the white dwarf has a strong magnetic field, cyclotron-resonance radiation pressure from photospheric radiation could drive the wind, with an estimated mass-loss rate $\approx 2 \times 10^{10}$ g s^{-1}. Thus, a hot magnetic white dwarf could emit X-rays from an optically thin thermal plasma in a radiation-driven outflow.

6.2. *Cyclotron Radiation*

The *Chandra* observation sets stringent constraints on a supposed hot corona above the white dwarf atmosphere. For GD 356, the X-ray luminosity $L_{\rm X} < 6.0 \times 10^{25}$ ergs s^{-1} and the electron number density $n_0 < 4.4 \times 10^{11}$ cm^{-3} at the base of a corona of (exponential) scale height of 2.0×10^7 cm for a 1 keV plasma. However, for a magnetic white dwarf, Zheleznyakov et al. (2004) note that electron-cyclotron emission lines and radiative losses even more severely constrain the parameters of a hypothesized hot corona.

For the 15 MG field of GD 356, we computed the radiative transfer in a hot corona, including cyclotron and bremsstrahlung emissivities and opacities due to cyclotron radiation (Chanmugam et al. 1989) and Faraday rotation and mixing. Figure 3 displays the emergent spectrum for white dwarf parameters appropriate to GD 356 (§ 4) and coronal density and temperatures given in the caption. For a density comparable to the upper limit set by the *Chandra* observation, the hypothesized hot corona would emit extremely strong thermal cyclotron lines in the near-infrared band, namely, around the second and third harmonics of the cyclotron frequency ($\nu_B = 42$ THz and $\lambda_B = 7.1$ μm). The *JHK* photometry (Skrutskie et al. 2006) shows no indication of such an excess, indicating that a hot corona does not exist or has a density much lower than the upper limit set by the X-ray observations. Alternatively, the magnetic field could be somewhat weaker than 15 MG, which would shift the strong third harmonic ($\nu_3 = 126$ THz and $\lambda_3 = 2.4$ μm) to a lower frequency, longward of the K_s band. Nevertheless, our calculation confirms the conclusion of Zheleznyakov et al. (2004): infrared–visible spectrophotometry is potentially a powerful probe of any hot corona around a magnetic white dwarf.

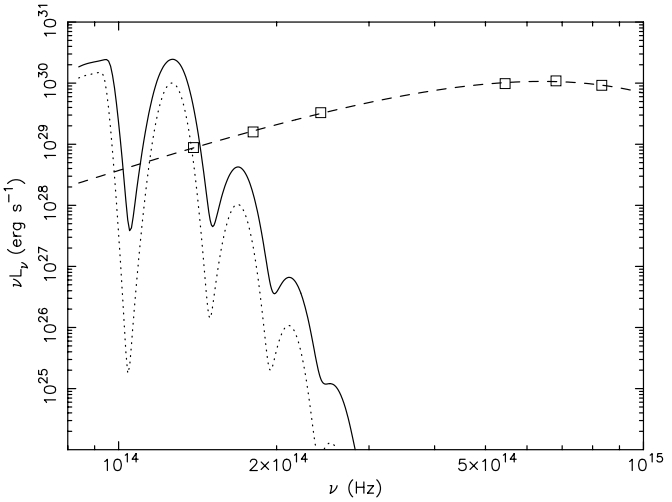

FIG. 3.—Emergent cyclotron spectrum from a hypothesized hot corona around GD 356, in comparison to a 7840 K photospheric spectrum (*dashed line*) and photometric data (*squares*). Calculations assume a 15 MG field at a mean viewing angle $\theta = \arctan(0.5) = 26.6^\circ$ and coronal parameters discussed in the text (§ 4), for a (coronal base) electron density $n_0 = 1 \times 10^{11}$ cm^{-3} and temperature $T = 1.5$ keV (*solid line*) or 1.0 keV (*dotted line*).

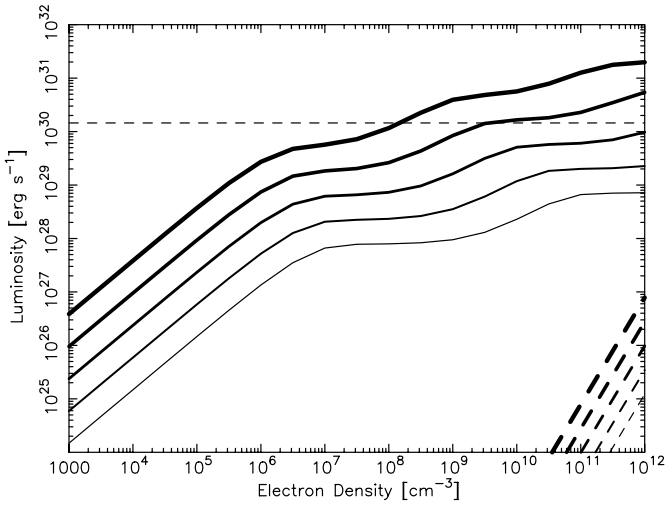

FIG. 4.—Contributors to the luminosity of a hypothetical corona around the magnetic white dwarf GD 356, in comparison to its photospheric luminosity (*horizontal thin dashed line*). Solid lines denote the thermal cyclotron luminosity for $B = 15$ MG and $kT = 0.125$, 0.25, 0.5, 1.0, and 2.0 keV, corresponding to increasing line thickness. Dashed lines denote the thermal bremsstrahlung luminosity for the same set of coronal temperatures.

In addition to producing potentially detectable emission lines, thermal cyclotron radiation would be the dominant cooling mechanism in a hot corona around a magnetic white dwarf. Figure 4 displays the radiated thermal cyclotron and bremsstrahlung luminosities for a supposed isothermal corona around GD 356 ($B =$ 15 MG), as a function of density, for various electron temperatures between 0.125 and 2.0 keV. As the plot clearly shows, cyclotron cooling dramatically exceeds bremsstrahlung cooling for a hot tenuous plasma above a magnetic white dwarf. Indeed, for GD 356, the coronal thermal cyclotron luminosity rivals the photospheric luminosity, unless the electron density is very much less than the upper limit set by the X-ray observation.

Strong cyclotron cooling above a magnetic white dwarf imposes severe demands on any coronal heating mechanism. As Figure 4 demonstrates, even the weak requirement (Zheleznyakov et al. 2004) that the coronal thermal cyclotron luminosity not exceed the photospheric luminosity limits the electron density to $n_0 < 3 \times 10^9$ cm^{-3} for $kT = 1$ keV. If a wave (or other magnetic energy) flux as large as 10^{10} ergs cm^{-2} s^{-1} (Musielak 1987) efficiently heats a corona around GD 356, this heating rate can balance cyclotron cooling for $n_0 \approx 3 \times 10^5$ cm^{-3} for $kT = 1$ keV. This is about 6 orders of magnitude less than the density limit set by X-ray nondetection.

For an electron density $n_0 < 3 \times 10^6$ cm^{-3}, approximately independent of temperature, a corona above the white dwarf photosphere would be transparent to cyclotron radiation in the 15 MG field of GD 356. However, when transparent, the cyclotron cooling time—again approximately independent of temperature—is only 2 μs in this magnetic field. For electron densities and temperatures of interest, the mean time between collisions, $\sim(1.4 \times 10^9$ s cm$^{-3})[kT/(1$ keV$)]^{1.5} n_e^{-1}$, is much longer than this cyclotron cooling time. Thus, the plasma would not be in local thermodynamic equilibrium (LTE; Zheleznyakov et al. 2004, and references therein), unless some collisionless process (e.g., scattering by Alfvén waves) intervenes to transfer energy to the electrons' transverse degrees of freedom on this very short timescale.

6.3. *Summary*

In summary, our *Chandra* observation of the single cool white dwarf GD 356 limits the luminosity and density of a hypothesized hot corona to $L_X < 6.0 \times 10^{25}$ ergs s^{-1} and $n_0 < 4.4 \times 10^{11}$ cm^{-3} (99.7% confidence), for a 1 keV thermal bremsstrahlung spectrum. We also re-analyzed archival *ROSAT* data for this white dwarf, G99-47, GD 90, G195-19, and WD 2316+123, as well as archival *Chandra* data for LHS 1038 and GD 358, using a statistical methodology (described in the Appendix) better suited to the low-count observations. Our upper limits are reasonably consistent with those of the original authors and lie somewhat above the limits we set for GD 356. As an aside to these searches for X-ray emission from cool white dwarfs, we have listed all *Chandra*-detected sources in the LHS 1038, GD 356, and GD 358 fields on the ACIS-S3 CCD.

We have shown (see also Zheleznyakov et al. 2004) that for magnetic white dwarfs (such as GD 356), the nondetection of infrared–visible cyclotron emission lines can more severely constrain the parameters for a hot corona than does an X-ray nondetection. Furthermore, strong cyclotron cooling places extreme demands on any coronal-heating mechanism. Indeed, our preliminary theoretical analysis suggests that cyclotron cooling around magnetic white dwarfs renders the formation and maintenance of a hot corona problematic. However, we require a more thorough study to prove this conclusively.

Those of us at NASA's Marshall Space Flight Center (MSFC) acknowledge support from the *Chandra* Program. V. E. Z. acknowledges support from the NASA Postdoctoral Program (NPP). We obtained the *Chandra* observation of GD 356 in response to proposal 5200156. Our analyses utilized software tools from the *Chandra* X-ray Center (operated for NASA by the Smithsonian Astrophysical Observatory, Cambridge, MA) and from the High-Energy Astrophysics Science Archive Research Center (HEASARC, operated by the NASA Goddard Space Flight Center, Greenbelt, MD, and by the Smithsonian Astrophysical Observatory, Cambridge, MA). In addition, our research utilized the SIMBAD database and VizieR catalog access tool (operated at Centre de Données astronomiques de Strasbourg, France) and NASA's Astrophysics Data System (operated by the Harvard-Smithsonian Center for Astrophysics, Cambridge, MA).

APPENDIX A

STATISTICAL METHODOLOGY

Statistical estimates of source and background counts and their errors often merely approximately describe an observation or apply only in the large-number limit. Here we present a statistical methodology that more generally describes apertured data (including allowing for uncertainty in the background) and makes no large-number assumption. First (§ A1), we obtain the probability distribution that accurately describes the observation and provides the basis for the statistical analyses to follow. We then describe an appropriate statistical test for detection of a source (§ A2) and one for constraining the expectation value for the number of source events (§ A3).

A1. PROBABILITY FOR OBSERVED EVENTS

We characterize a measurement (realization) in terms of the observed number of events (counts) m_T and m_R in disjoint regions (apertures) T and R of known measure (solid angle, area, wavelength band, time interval, etc., as appropriate) Ω_T and Ω_R, respectively. We regard T as a "Target" aperture that *may* contain a source with an expectation value $\bar{m}_S$ for the number of events (counts), and R as a "Reference" aperture that contains *no* source. Although no source lies within R, source events may occur in R if their distribution is not delta-distributed, i.e., confined to a point. Thus, we define Ψ_T and Ψ_R to be the known fractions of source events in the Target T and Reference R apertures, such that the expectation values for the number of source events are $\bar{m}_S\Psi_T$ and $\bar{m}_S\Psi_R$, respectively. In addition to source events, apertures T and R contain background (nonsource) events, with expectation values $\bar{\mu}_B\Omega_T$ and $\bar{\mu}_B\Omega_R$, with $\bar{\mu}_B$ the expectation value for the density (per unit measure) of background events. For convenience, we denote with a subscripted "U" parameters or values over the combined aperture $U \equiv T \cup R$, with $T \cap R = 0$, namely, $\Omega_U = \Omega_T + \Omega_R$, $\Psi_U = \Psi_T + \Psi_R$, and $m_U = m_T + m_R$.

Consequently, the expectation values for the number of events (counts) in apertures T and R are $\bar{m}_T$ and $\bar{m}_R$, respectively:

$$\bar{m}_T = \bar{m}_S\Psi_T + \bar{\mu}_B\Omega_T, \tag{A1}$$

$$\bar{m}_R = \bar{m}_S\Psi_R + \bar{\mu}_B\Omega_R. \tag{A2}$$

Hence, the probability for m_T and m_R events in an observation (realization) is

$$P_{m_T,m_R}(\bar{m}_T,\bar{m}_R) = \left(\bar{m}_T^{m_T}e^{-\bar{m}_T}/m_T!\right)\left(\bar{m}_R^{m_R}e^{-\bar{m}_R}/m_R!\right). \tag{A3}$$

On substituting equations (A1) and (A2) into equation (A3), we get

$$P_{m_T,m_R}(\bar{m}_S,\bar{\mu}_B;\Psi_T,\Psi_R,\Omega_T,\Omega_R) = \left[(\bar{m}_S\Psi_T + \bar{\mu}_B\Omega_T)^{m_T}e^{-(\bar{m}_S\Psi_T+\bar{\mu}_B\Omega_T)}/m_T!\right] \times \left[(\bar{m}_S\Psi_R + \bar{\mu}_B\Omega_R)^{m_R}e^{-(\bar{m}_S\Psi_R+\bar{\mu}_B\Omega_R)}/m_R!\right]. \tag{A4}$$

Given values for the known parameters (Ψ_T, Ψ_R, Ω_T, and Ω_R) and for the observed number of events (m_T and m_R) in each aperture, equation (A4) provides the basis for statistical tests to constrain expectation values for source events ($\bar{m}_S$) and background event density ($\bar{\mu}_B$).

A2. DETECTION OF A SOURCE

The first type of statistical test addresses detection. Note that this is a test for *detection* only: it provides neither a measured value nor an upper limit. In order to test for detection of a source in the target aperture T, we investigate the hypothesis that there is *no source*, i.e., that $\bar{m}_S = 0$. Under this null hypothesis, the conditional probability of obtaining m_T and m_R (background) events in apertures T and R, given $m_U \equiv m_T + m_R$ events in both apertures, is

$$P_{m_T,m_R}(0,\bar{\mu}_B;\Omega_T,\Omega_R|m_U) = P_{m_T,m_R}(0,\bar{\mu}_B;\Omega_T,\Omega_R)/P_{m_U}(0,\bar{\mu}_B;\Omega_U), \tag{A5}$$

with $\Omega_U \equiv \Omega_T + \Omega_R$. From the Poisson distribution (eq. [A4]), the conditional probability (eq. [A5]) reduces to the obvious binomial distribution, independent of $\bar{\mu}_B$ under the null hypothesis,

$$P_{m_T,m_R}(\Omega_T,\Omega_R|m_U;\bar{m}_S=0) = P_{m_T,m_R}(\Omega_T,\Omega_R)/P_{m_U}(\Omega_U) = \left(\frac{\Omega_T^{m_T}}{m_T!}\right)\left(\frac{\Omega_R^{m_R}}{m_R!}\right)\Big/\left(\frac{\Omega_U^{m_U}}{m_U!}\right) = \frac{m_U!}{m_T!m_R!}\left(\frac{\Omega_T}{\Omega_U}\right)^{m_T}\left(\frac{\Omega_R}{\Omega_U}\right)^{m_R}. \tag{A6}$$

The cumulative probability of obtaining m_T or more events in the Target aperture T, given $\bar{m}_S = 0$ and $m_U = m_T + m_R$ events in the combined aperture $\Omega_U = \Omega_T + \Omega_R$ is then

$$\mathcal{P}(\geq m_T|m_U;\bar{m}_S=0) = \sum_{m=m_T}^{m_U}\frac{m_U!}{m!(m_U-m)!}\left(\frac{\Omega_T}{\Omega_U}\right)^m\left(1-\frac{\Omega_T}{\Omega_U}\right)^{m_U-m}. \tag{A7}$$

Consequently, equation (A7) gives a confidence level $\mathcal{C}$ for detection of a source, i.e., for showing that $\bar{m}_S > 0$:

$$\mathcal{C}(\bar{m}_S > 0|m_T, m_R; \Omega_T, \Omega_R) = \mathcal{P}(<m_T|m_U; \bar{m}_S = 0) = 1 - \mathcal{P}(\geq m_T|m_U; \bar{m}_S = 0)$$
$$= \sum_{m=0}^{m_T-1} \frac{m_U!}{m!(m_U - m)!} \left(\frac{\Omega_T}{\Omega_U}\right)^m \left(1 - \frac{\Omega_T}{\Omega_U}\right)^{m_U - m}. \quad \text{(A8)}$$

This expression is valid for any number of events in either the Target or the Reference aperture. Thus, it does not require that the background event density (μ_B) be statistically well determined.

If the expectation value for the background event density is well known, then we can simplify equation (A4) to the more familiar

$$P_{m_T}(0, \mu_B; \Omega_T) = \frac{(\mu_B \Omega_T)^{m_T}}{m_T!} e^{-\mu_B \Omega_T}. \quad \text{(A9)}$$

Given μ_B, the corresponding cumulative probability of obtaining m_T or more (background) events in the Target aperture then becomes

$$\mathcal{P}(\geq m_T|\mu_B \Omega_T; \bar{m}_S = 0) = \sum_{m=m_T}^{\infty} \frac{(\mu_B \Omega_T)^m}{m!} e^{-\mu_B \Omega_T}. \quad \text{(A10)}$$

Therefore, equation (A10) yields a confidence level $\mathcal{C}$ for detection of a source, i.e., for showing that $\bar{m}_S > 0$:

$$\mathcal{C}(\bar{m}_S > 0|m_T; \mu_B \Omega_T) = \mathcal{P}(<m_T|\mu_B \Omega_T; \bar{m}_S = 0) = 1 - \mathcal{P}(\geq m_T|\mu_B \Omega_T; \bar{m}_S = 0)$$
$$= \sum_{m=0}^{m_T-1} \frac{(\mu_B \Omega_T)^m}{m!} e^{-\mu_B \Omega_T}. \quad \text{(A11)}$$

A3. MEASUREMENT OF SOURCE

The second type of statistical test addresses measurement of the expectation value $\bar{m}_S$ for the number of source events. Using equation (A4) as a likelihood function for the parameters m_S and μ_B, we obtain maximum-likelihood estimators for each,

$$\hat{m}_S = \frac{m_T \Omega_R - m_R \Omega_T}{\Psi_T \Omega_R - \Psi_R \Omega_T}, \quad \text{(A12)}$$

$$\hat{\mu}_B = \frac{m_R \Psi_T - m_T \Psi_R}{\Psi_T \Omega_R - \Psi_R \Omega_T}. \quad \text{(A13)}$$

Evaluation of the second-order partial derivatives of these parameters about their maximum-likelihood estimators leads to estimators for the components of the covariance matrix,

$$\hat{\sigma}^2_{m_S} = \mathrm{Cov}(m_S, m_S) = \left(\frac{\Psi_T^2}{m_T} + \frac{\Psi_R^2}{m_R}\right)^{-1}, \quad \text{(A14)}$$

$$\hat{\sigma}^2_{\mu_B} = \mathrm{Cov}(\mu_B, \mu_B) = \left(\frac{\Omega_T^2}{m_T} + \frac{\Omega_R^2}{m_R}\right)^{-1}, \quad \text{(A15)}$$

$$\hat{\sigma}_{m_S, \mu_B} = \mathrm{Cov}(m_S, \mu_B) = \left(\frac{\Psi_T \Omega_T}{m_T} + \frac{\Psi_R \Omega_R}{m_R}\right)^{-1}. \quad \text{(A16)}$$

Here, $\hat{\sigma}_{m_S}$ and $\hat{\sigma}_{\mu_B}$ are the maximum-likelihood estimators for the standard deviation in m_S and μ_B and $\sigma_{m_S, \mu_B} \neq 0$ shows that the estimators for m_S and μ_B are correlated.

Equations (A14), (A15), and (A16) do not accurately describe the probability distribution for m_S and μ_B except in the large-number limit, i.e., when the probability is approximately normally distributed. Thus, to obtain an accurate description of the probability density function for m_S and μ_B, we return to equation (A4).

Equation (A4) gives the probability for m_T and m_R events in apertures T and R, given the expectation values $\bar{m}_S$ and $\bar{\mu}_B$, i.e., $P_{m_T, m_R}(\bar{m}_S, \bar{\mu}_B) = P(m_T, m_R|\bar{m}_S, \bar{\mu}_B)$. From this, one constructs a probability density function describing the (normalized) likelihood for the expectation values, given the observed distribution of events, i.e., $p(m_S, \mu_B|m_T, m_R)$. In order to facilitate this construction, we rewrite equation (A4), after slightly redefining variables and constant coefficients, as

$$P(m_T, m_R|\nu_S, \nu_B) = \frac{(\psi_T \nu_S + \omega_T \nu_B)^{m_T}}{m_T!} \frac{(\psi_R \nu_S + \omega_R \nu_B)^{m_R}}{m_R!} e^{-(\nu_S + \nu_B)}. \quad \text{(A17)}$$

The new variables are the expectation value for the number of source events in both apertures combined, $\nu_S \equiv \Psi_U m_S = (\Psi_T + \Psi_R) m_S$, and the expectation value for the number of background events in both apertures combined, $\nu_B \equiv \Omega_U \mu_B = (\Omega_T + \Omega_R) \mu_B$. The new

(constant, predetermined) coefficients are the expected fractions of total source events in apertures T and R, $\psi_T \equiv \Psi_T/\Psi_U = \Psi_T/(\Psi_T + \Psi_R)$ and $\psi_R \equiv \Psi_R/\Psi_U = \Psi_R/(\Psi_T + \Psi_R)$, respectively, and the expected fractions of total background events in apertures T and R, $\omega_T \equiv \Omega_T/\Omega_U = \Omega_T/(\Omega_T + \Omega_R)$ and $\omega_R \equiv \Omega_R/\Omega_U = \Omega_R/(\Omega_T + \Omega_R)$, respectively. Thus, $\psi_T + \psi_R = 1$, so that ψ_T or ψ_R is the probability that a given source event occurs in aperture T or R, respectively. Analogously, $\omega_T + \omega_R = 1$, so that ω_T or ω_R is the probability that a given background event occurs in aperture T or R, respectively. Expanding equation (A17) in terms of a double binomial series, we obtain

$$P(m_T, m_R|\nu_S, \nu_B) = \sum_{i=0}^{m_T}\sum_{j=0}^{m_R} \frac{\psi_T^i \psi_R^{m_R-j}}{i!(m_R-j)!}\frac{\omega_R^j \omega_T^{m_T-j}}{j!(m_T-i)!}\nu_S^{i+m_R-j}\nu_B^{j+m_T-i}e^{-(\nu_S+\nu_B)}. \tag{A18}$$

Dividing equation (A18) by the partition function $Z(m_T, m_R)$—equivalent to normalizing the (unweighted; cf. Kraft et al. 1991) integral of $P(m_T, m_R|\nu_S, \nu_B)$ over all possible values $(0, \infty)$ of ν_S and ν_B—we derive the desired probability density function

$$\begin{aligned} p(\nu_S, \nu_B|m_T, m_R) &= \frac{P(m_T, m_R|\nu_S, \nu_B)}{Z(m_T, m_R)} \\ &= \frac{1}{Z(m_T, m_R)}\sum_{i=0}^{m_T}\sum_{j=0}^{m_R} \frac{\psi_T^i \psi_R^{m_R-j}}{i!(m_R-j)!}\frac{\omega_R^j \omega_T^{m_T-j}}{j!(m_T-i)!}\nu_S^{i+m_R-j}\nu_B^{j+m_T-i}e^{-(\nu_S+\nu_B)}, \end{aligned} \tag{A19}$$

where the partition function

$$Z(m_T, m_R) = \sum_{i=0}^{m_T}\sum_{j=0}^{m_R} \frac{(i+m_R-j)!}{i!(m_R-j)!}\psi_T^i \psi_R^{m_R-j}\frac{(j+m_T-i!)}{j!(m_T-i)!}\omega_R^j \omega_T^{m_T-i}. \tag{A20}$$

Note that the partition function (eq. [A20]) is the a priori probability that, given $m_U = m_T + m_R$ total (source and background) events, m_T and m_R events occur in apertures T and R, respectively.

We may integrate the probability density $p(\nu_S, \nu_B|m_T, m_R)$ from equations (A19) and (A20) to constrain jointly the values of ν_S and ν_B at a specified confidence level $\mathcal{C}$. Alternatively, we may constrain either parameter individually, after integrating over the other's full range $(0, \infty)$. Thus, the probability density for the expectation value ν_S of the number of source events in the combined aperture $(U \equiv T \cup R)$, without regard to the value of ν_B, is

$$p(\nu_S|m_T, m_R) = \frac{1}{Z(m_T, m_R)}\sum_{i=0}^{m_T}\sum_{j=0}^{m_R} \frac{(j+m_T-i)!}{j!(m_T-i)!}\omega_R^j \omega_T^{m_T-i}\frac{\nu_S^{i+m_R-j}e^{-\nu_S}}{i!(m_R-j)!}\psi_T^i \psi_R^{m_R-j}. \tag{A21}$$

For example, to establish an upper limit to the expectation value $\bar{\nu}_S$ (without regard to ν_B) at a confidence level $\mathcal{C}$, one solves

$$\begin{aligned} 1 - \mathcal{C}(\bar{\nu}_S < \nu_S|m_T, m_R) &= \int_{\nu_S}^{\infty} p\left(\nu_S'|m_T, m_R\right) d\nu_S' \\ &= \frac{1}{Z(m_T, m_R)}\sum_{i=0}^{m_T}\sum_{j=0}^{m_R} \frac{(j+m_T-i)!}{j!(m_T-i)!}\omega_R^j \omega_T^{m_T-i}\frac{\Gamma(i+m_R-j+1, \nu_S)}{i!(m_R-j)!}\psi_T^i \psi_R^{m_R-j}, \end{aligned} \tag{A22}$$

where $\Gamma(n+1, \nu)$ is the (upper) incomplete gamma function.

In the special case that $\psi_T \to 1$ and $\psi_R \to 0$, i.e., the expected fraction of source events in the reference aperture is negligible, the double sum reduces to the single sum

$$\begin{aligned} 1 - \mathcal{C}(\bar{\nu}_S < \nu_S|m_T, m_R) &\xrightarrow{\psi_R \to 0} \frac{1}{Z(m_T, m_R)}\sum_{i=0}^{m_T} \frac{(m_R+m_T-i)!}{m_R!(m_T-i)!}\omega_R^{m_R}\omega_T^{m_T-i}\frac{\Gamma(i+1, \nu_S)}{i!} \\ &= \frac{1}{Z(m_T, m_R)}\sum_{k=0}^{m_T} \frac{(m_R+k)!}{m_R!k!}\omega_R^{m_R}\omega_T^{k}\frac{\Gamma(m_T-k+1, \nu_S)}{(m_T-k)!}. \end{aligned} \tag{A23}$$

The partition function also reduces to a single sum, namely,

$$Z(m_T, m_R) \xrightarrow{\psi_R \to 0} \sum_{i=0}^{m_T} \frac{(m_R+m_T-i)!}{m_R![m_T-i]!}\omega_R^{m_R}\omega_T^{m_T-i} = \sum_{k=0}^{m_T} \frac{(m_R+k)!}{m_R!k!}\omega_R^{m_R}\omega_T^{k}. \tag{A24}$$

REFERENCES

Arcoragi, J.-P., & Fontaine, G. 1980, ApJ, 242, 1208
Arnaud, K. A., Zheleznyakov, V. V., & Trimble, V. 1992, PASP, 104, 239
Barstow, M. A., et al. 1993, MNRAS, 264, 16
Bespalov, P. A., & Zheleznyakov, V. V. 1990, Soviet Astron. Lett., 16, 442
Boese, F. G. 2000, A&AS, 141, 507
Böhm, K. H., & Cassinelli, J. 1971, A&A, 12, 21
Cavallo, R., Arnaud, K. A., & Trimble, V. 1993, J. Astrophys. Astron., 14, 141
Chanmugam, G., Barrett, P. E., Wu, K., & Courtney, M. W. 1989, ApJS, 71, 323
Fleming, T. A., Werner, K., & Barstow, M. A. 1993, ApJ, 416, L79

Fontaine, G., Montmerle, T., & Michaud, G. 1982, ApJ, 257, 695
Greenstein, J. L., & McCarthy, J. K. 1985, ApJ, 289, 732
Jordan, S. 2001, in ASP Conf. Ser. 226, 12th European Workshop on White Dwarfs, eds. J. L. Provencal, H. L. Shipman, J. MacDonald, & S. Goodchild (San Francisco: ASP), 269
Kahn, S. M., Wesmael, F., Liebert, J., Raymond, J. C., Steiner, J. E., & Shipman, H. L. 1984, ApJ, 278, 255
Kawaler, S., Sekii, T., & Gough, D. 1999, ApJ, 516, 349
Kidder, K. M., Holberg, J. B., Barstow, M. A., Tweedy, R. W., & Wesmael, F. 1992, ApJ, 394, 288
Koester, D. 2002, A&A Rev., 11, 33
Koester, D., Beuermann, K., Thomas, H.-C., Graser, U., Giommi, P., & Tagliaferri, G. 1990, A&A, 239, 260
Kraft, R. P., Burrows, D. N., & Nousek, J. A. 1991, ApJ, 374, 344
Li, J., Wickramasinghe, D. T., & Ferrario, L. 1998, ApJ, 503, L151
McCook, G. P., & Sion, E. M. 1999, ApJS, 121, 1
Mermilliod, J.-C., & Mermilliod, M. 1994, Catalog of Mean *UBV* Data on Stars (New York: Springer)
Mewe, R., Heise, J., Gronenschild, E. H. B. M., Brinkman, A. C., Schrijver, J., & den Boggende, A. J. F. 1975, Nature, 256, 711
Monet, D. G., et al. 2003, AJ, 125, 984
Musielak, Z. E. 1987, ApJ, 322, 234
Musielak, Z. E., & Fontenla, J. M. 1989, ApJ, 346, 435
Musielak, Z. E., Noble, M., Porter, J. G., & Winget, D. E. 2003, ApJ, 593, 481
Musielak, Z. E., Porter, J. G., & Davis, J. M. 1995, ApJ, 453, L33
Musielak, Z. E., Winget, D. E., & Montgomery, M. H. 2005, ApJ, 630, 506
Paerels, F. B. S., & Heise, J. 1989, ApJ, 339, 1000
Petre, R., Shipman, H. L., & Canizares, C. R. 1986, ApJ, 304, 356
Provencal, J. L., Shipman, H. L., & MacDonald, J. 2005, ApJ, 627, 418
Schmidt, G. D., & Smith, P. S. 1995, ApJ, 448, 305
Serber, A. V. 1990, Soviet Astron., 34, 291
Shipman, H. L. 1976, ApJ, 206, L67
Skrutskie, M. F., et al. 2006, AJ, 131, 1163
Tennant, A. F. 2006, AJ, 132, 1372
Thomas, J. H., Markiel, J. A., & Van Horn, H. M. 1995, ApJ, 453, 403
Ulmschneider, P. 2003, in Lectures on Solar Physics, eds. H. M. Antia, A. Bhatnagar, & P. Ulmschneider (New York: Springer), 232
van Altena, W. F., Lee, J. T., & Hoffleit, E. D. 1995, The General Catalogue of Trigonometric Stellar Parallaxes (4th ed.; New Haven: Yale Univ. Observatory)
Wesmael, F., Auer, L. H., Van Horn, H. M., & Savedoff, M. P. 1980, ApJS, 43, 159
Winget, D. E., et al. 1994, ApJ, 430, 839
Zheleznyakov, V. V., Koryagin, S. A., & Serber, A. V. 2004, Astron. Rep., 48, 121
Zheleznyakov, V. V., & Litvinchuk, A. A. 1984, Ap&SS, 105, 73
Zheleznyakov, V. V., Serber, A. V., & Kuijpers, J. 1996, A&A, 308, 465